Structural and Compositional Analyses of Thin Film Manganese-Doped Zinc Sulfide Using Transmission Electron Microscopy Techniques

Yoshimitsu ISHIKAWA
Shinji HIGUCHI
Yasuo NAKANISHI

The microstructure and elemental composition of a thin film microcrystal of manganese-doped zinc sulfide (ZnS:Mn), a material used in electroluminescent (EL) devices was investigated by transmission electron microscopes (TEM). Lattice defects were observed by the high-resolution TEM image, whereas the lattice strain induced by the lattice defects was observed by the large-angle convergent beam electron diffraction (LACBED) pattern. The unit cell dimensions of a region containing the lattice defects were determined by the convergent beam electron diffraction (CBED) patterns, with compositional analyses of the lattice defects being performed by energy dispersive X-ray spectrometry (EDS). EDS compositional analyses were also performed on the grain boundaries. The causes of ZnS crystal imperfections and of elemental composition variations are discussed.

1. Introduction

The discovery of electroluminescence (EL) in 1936[1] led to numerous studies directed at elucidating and utilizing this unique phenomenon,[2] with one important application being the EL flat panel display. A variety of inorganic and organic compounds have been examined for use as an EL material, and manganese-doped zinc sulfide (ZnS:Mn) is the most commonly investigated of these.

In addition to zinc sulfide's EL applications, its crystallographic structure has also been widely researched. ZnS has two polytype structures, i. e., the zinc-blende and the wurtzite structures. Since the polytype is formed during crystal growth by changes in the bonding patterns between atoms, the productions of resultant lattice defects also tends to be affected by these changes. The lattice defects in ZnS bulk crystal have been investigated in detail by a high-resolution transmission electron microscope (HRTEM); thereby enabling the resultant stacking faults and microtwins to be clearly characterized.[3,4]

Practical-use EL devices utilize thin films. However, as the crystals grow in ZnS films, the crystal structure changes (lattice defects) caused by the stacking faults and microtwin structures induce lattice strain, hence making the EL device inferior. Existing defects in EL thin films are believed to inhibit effective EL light emission because the electron band width becomes narrower; thus causing the emitted light to be scattered and resulting in an inefficient EL device. It is also commonly known that electrons in the electric field are trapped in the defects, therefore the EL device loses efficiency because the electrons reaching the center of the light emission are reduced. Since lattice strain distorts the electronic band structure, luminescence intensity changes occur. However, few detailed microscopic studies have been performed for EL devices from a lattice defect and lattice strain perspective, but have instead focused an either a thin film's grain size or shape. As a result, the relationship between the film's microscopic structure and physical properties has not been clarified.

Analyses of lattice defects and lattice strain by transmission electron microscope (TEM) have recently been perfomed using the convergent beam electron diffractions (CBED).[5] The CBED analysis method is advantageous to characterize microcrystals because the exposed electron beam is converged onto the specimen surface while the CBED pattern is under observation, being especially useful and effective for thin film samples. Additionally, the large-angle convergent beam electron diffraction (LACBED) method[6] is advantageous for lattice strain analysis because real space and reciprocal space information can be simultaneously obtained.

This led to the present study which describes analysis results of lattice defects and lattice strain for ZnS:Mn thin films using an HRTEM image and LACBED pattern, respectively. Lattice parameters in lattice defect regions were determined by comparisons between observed and simulated CBED patterns, with results showing only slight variations in actual lattice parameters. Compositional analyses were performed by energy dispersive X-ray spectrometry (EDS) in order to discuss the stoichiometry of the lattice defects.

2. Experimental Methods

The ZnS:Mn thin film samples under investigation were prepared by deposition on a glass substrate. The film for HRTEM observations was produced by electron beam (EB) vacuum deposition, whereas the film for EDS experiments and CBED pattern observations was obtained by metal organic chemical vapor deposition (MOCVD).

The TEM specimens were prepared to allow a cross sectional view to be observed. The samples were comprised of two films glued face-to-face with epoxy resin, sliced with a disc cutter to ~500 μm, ground and polished normal to the surface to an approximately 50 μm thickness, and then thinned by ion beam etching. Conventional TEM experiments were carried out by a JEM-2000FX (JEOL) TEM set at a 200 kV accelerating voltage, while high-resolution TEM observations utilized a JEM-2000EX (JEOL) TEM with the same 200 kV accelerating voltage. An energy dispersive X-ray spectrometer (EDS, TN5500, Noran) was attached to the JEM-2000FX TEM for experiments to facilitate semiquantitative elemental analyses. The irradiation area of the EDS measurements was nearly 30 nm except for the examination to study the influence of ion beam etching.

3. Results and Discussion

Figure 1(a) shows a cross-sectonal view of the EB deposition sample, where columnar crystal growth is apparent (grain size: ~0.1 μm dia.). The grain is almost the same size from the film-substrate boundary to the surface, with numerous "scratched" defect-like patterns appearing. Figure 1(b) shows the sample's cross-sectional view by MOCVD. Notice the columnar crystal growth is also present (grain size: ~0.15 μm dia.), although the grain is not as tall as the one shown by EB deposition and few grains have grown from the substrate to the sur-

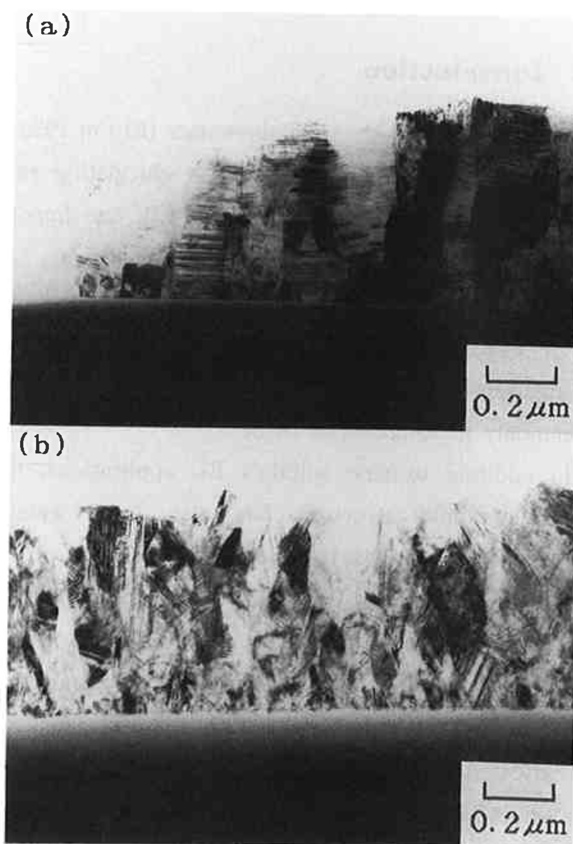

Fig. 1 TEM images of the samples in a cross-sectional view made by (a) EB deposition and (b) MOCVD.

face. Also similar are the numerous defect-like patterns which can be seen. Since the EB deposition showed defect-like patterns (Fig. 1(a)) with point in the same directions and occur throughout the image, this regularity indicates that the sample's defects run in the same direction. HRTEM microstructure observations were taken on this sample, because the defects existed all over the thin film. On the other hand, EDS compositional analyses were performed on the MOCVD sample (Fig. 1(b)) because the positional difference between the perfect crystal region and the defect region is clear; thereby enabling this feature to be investigated.

〔1〕 HRTEM Observations

Figure 2 shows an HRTEM image of the EB deposition sample shown in Fig. 1(a), with the inset being a selected-area electron diffraction pattern taken simultaneously. This diffraction pattern can be interpreted as shown in Fig. 3,[4] where the diffraction spot indices are also indicated in Figs. 3(b) and (c). An almost equivalent distance exists from the direct beam spot to the 002 spot of the wurtzite structure and to the $1\bar{1}1$ spot of the zinc-blende one. Shuyuan *et al.*[4] showed using the diffraction pattern of a ZnS:Mn bulk crystal that the wurtzite structure coexists with the ZnS:Mn bulk crystal when high-temperature sintering is performed. However, since the 001 and the 010 spots can not be seen on the Fig. 3(a) diffraction pattern, the crystal must only contain the ZnS zinc-blende structure. The additional spots shown beside the $\bar{1}11$ and 002 spots in Fig. 3(a) are interpreted as representing a 180° rotation twin in the sample (Fig. 3(d)).

The Fig. 2 HRTEM image supports this finding, i. e., the wurtzite structure taken along [100] direction is expected to have a zig-zag orientation of bright spots because the cavities form a zig-zag orientation (Fig. 3(c)), whereas the zinc-blende structure (Fig. 3(b)) taken along the [110] direction is expected to have a corresponding linear orientation. Since the spots in Fig. 2 are on a straight line, the crystal contains only the zinc-blende structure. With respect to the HRTEM image, agreement is necessary between the position of the bright spots and the position of the

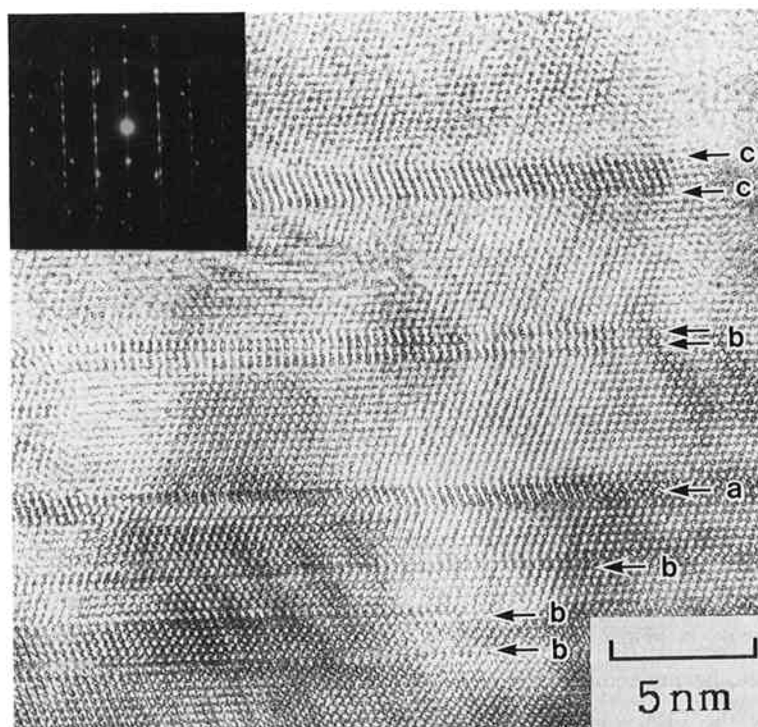

Fig. 2 ZnS:Mn HRTEM image viewed along the [110] direction of a zinc-blende structure. The inset shows a selected-area electron diffraction pattern simultaneously take on the same sample.

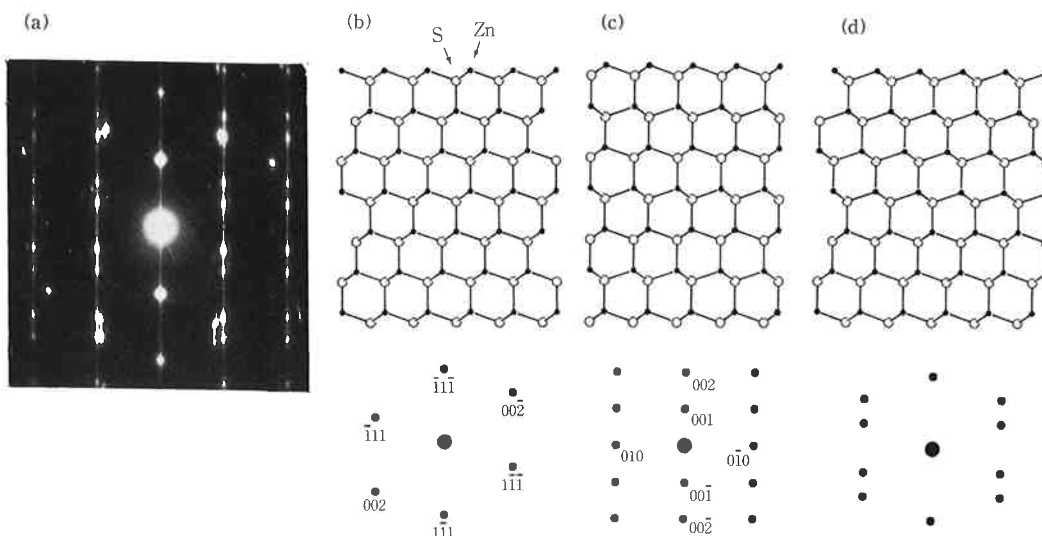

Fig. 3 ZnS diffraction pattern interpretations. (a) experimental diffraction pattern, (b) zinc-blende structure projected along the [110] direction and the diffraction pattern having a [110] direction of incidence, (c) wurtzite structure projected along the [100]direction and the diffraction pattern having a [100] direction of incidence, and (d) 180° rotation twin of the zinc-blende structure projected along the [110] direction.

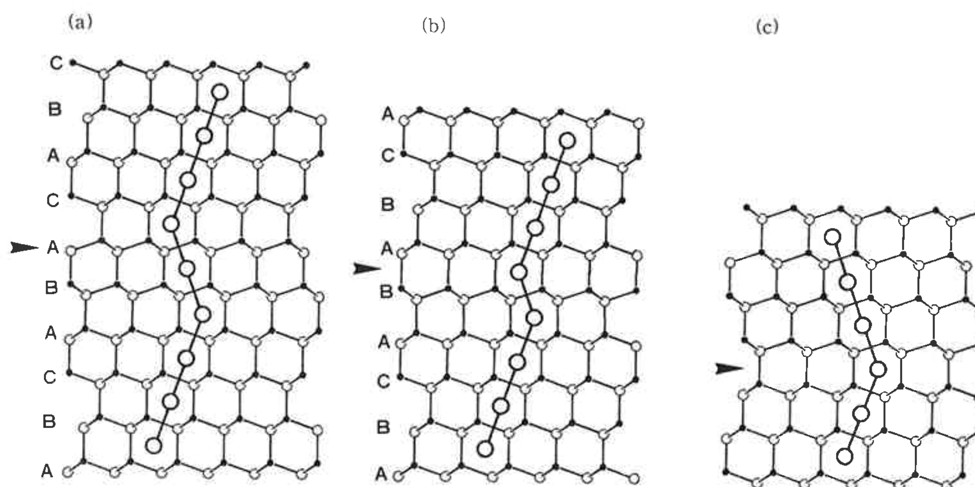

Fig. 4 ZnS structural model viewed along the [110]direction of a zinc-blende structure (a) extrinsic stacking fault, (b) intrinsic stacking fault, and (c) 180° rotation twin. The arrows indicate the stacking fault's position or twinning plane.

cavity in the structural model identified via HRTEM image simulation. The Fig. 2 diffraction pattern also has streaks where the spots are linked; thereby indicating the crystal's short coherency in the [1$\bar{1}$1] direction, i. e., the direction of crystal growth. The structural models shown in Fig. 4(a)-(c) of a zinc-blende ZnS structure, having some lattice defects which are viewed along the [110] direction, respectively represent an intrinsic stacking fault, extrinsic stacing fault, and 180° rotation twin. These defects are observed in the Fig. 2 HRTEM image, and are annotated by "a", "b", and "c" which respectively correspond to the three models in Fig. 4. Based on this, the defect-like patterns in the grains shown in Fig. 1 are considered to be lattice defects, with the previously mentioned short coherency being consistent with this conclusion. Since the lattice defects run across the direction of crystal growth, the grain is believed to consist of many stacked plate-like crystals that are cut-off by the defects.

[2] EDS Compositional Analyses

Before conducting an analysis of the film to in-

vestigate the influence of preparatory ion beam etching on the sample's elemental composition, compositional analysis was performed on several areas of various thickness. **Table 1** gives X-ray intensities from a ZnS:Mn on a thin film using an ~750 nm wide beam. Since the beam exposed the entire film, all possibel X-rays were generated. This experiment examined the overall thin film composition, and while the absolute element quantity at each position is not definitely known, the given ratios of S and Mn to Zn which existed at the position exposed by the electron beam can be obtained via this intensity ratio. Position 1 and 5 were most thin, and thus they were damaged the most by the ion beam etching. The compositional ratio of the sulfur atoms is smallest at the thinnest thickness due to the sulfur atom selectivity which occurs in ion beam etching. This selectivity is believed to be caused by either the Coulomb interaction between the sulfur anion and the argon cation, or by the difference of scattering cross-sections related to the ion radius of the longer sulfur anion (S^{2-}: 1.70 Å) to that of the zinc cation (Zn^{2+}: 0.74 Å).[7,8] A comparison of the elemental composition must therefore be performed on a region having the same thickness because different thicknesses will be damaged differently by ion beam etching; hence resulting in variable elemental compositions.

Table 1 Observed characteristic X-ray intensity variations from ZnS:Mn thin films using a ~750 nm wide beam.

Position[a]	Zn	S	Mn
1	3074	2694 (0.876)[b]	81 (0.026)
2	897	905 (1.009)	18 (0.020)
3	2050	1955 (0.954)	52 (0.025)
4	1474	1479 (1.003)	28 (0.019)
5	543	503 (0.926)	13 (0.024)
6	1455	1344 (0.924)	26 (0.018)
7	1223	1158 (0.947)	26 (0.021)

a) Positions 1-4 and 5-7 were taken from the same thin film, with positions 1 and 5 being the thinnest.
b) The values in parentheses were values normalized by the observed Zn X-ray intensities.

Compositional differences in the same grain were investigated, with **Table 2** listing the X-ray intensities from a ZnS:Ms thin film crystal which was exposed by 30 nm diameter convergent electron beam. To avoid the influence from the defects, the convergent electron beam was directed at positions having no defects. Positional diférences in elemental composition are accounted for by the resultant compositional differences among the last (upper), the middle (center), and the first (lower) period of the crystal growth. Results indicate that in the last period, not many sulfur atoms are present; once again supporting the conclusion the sulfur atoms are etched preferentially during ion beam etching.

Grain boundary compositional analysis results are summarized in **Table 3** along with those from the grain center. The sulfur amount is almost the same at the grain boundary and center, and no additional elements were detected at the grain boundary.

Table 2 Observed X-ray intensity variations in a thin film ZnS:Mn crystal.

Crystal	Zn	S Upper[a]	Mn	Zn	S Center[a]	Mn	Zn	S Lower[a]	Mn
1	294	239 (0.813)[b]	4 (0.014)	491	427 (0.870)	9 (0.019)	427	377 (0.883)	6 (0.014)
2	271	225 (0.830)	4 (0.015)	321	278 (0.866)	5 (0.016)	345	302 (0.875)	4 (0.012)
3	187	142 (0.759)	4 (0.021)	179	156 (0.872)	5 (0.028)	199	164 (0.824)	3 (0.015)
4	239	201 (0.841)	3 (0.015)	211	183 (0.867)	3 (0.014)	156	131 (0.840)	4 (0.026)
5	109	87 (0.798)	4 (0.037)	118	97 (0.822)	3 (0.025)	132	113 (0.856)	4 (0.030)
$\bar{x}$[c]		0.808	0.020		0.859	0.020		0.856	0.018
σ[d]		0.029	0.009		0.019	0.005		0.022	0.006

a) Crystal position values are from the same grain, however, the exposed beam was positioned either near the surface (upper), at the middle (center), or near the substrate (lower) part of the thin film cross-secton.
b) Values in parentheses were normalized by the observed Zn X-ray intensities.
c) $\bar{x}$ is the averaged intensity normalized by the Zn intensities for S and Mn.
d) σ is the standard deviation of these values.

Table 3 Observed X-ray intensity variations between grain boundary and center of grain in a ZnS:Mn thin film crystal.

Position[a)]	Zn	S	Mn	Zn	S	Mn
	Grain Boundary			Center of Grain		
1	364	343 (0.942)[b)]	7 (0.019)	327	334 (1.021)	6 (0.018)
2	262	235 (0.897)	6 (0.023)	210	195 (0.929)	6 (0.029)
3	260	210 (0.808)	5 (0.019)	244	183 (0.750)	5 (0.020)
4	1187	1030 (0.868)	23 (0.019)	1038	796 (0.767)	24 (0.023)
5	1666	1589 (0.954)	27 (0.016)	1799	1638 (0.911)	29 (0.016)
$\bar{x}$[c)]		0.894	0.019		0.876	0.021
σ		0.053	0.002		0.103	0.004

a) Position values are from regions having approximately the same thickness respectively.
b) Values in parentheses were normalized by the observed Zn X-ray intesities.
c) $\bar{x}$ and σ are the same as in Table 2.

Table 4 Observed X-ray intensity variations between on lattice defect and on perfect crystal region in a ZnS:Mn thin film crystal.

Crystal[a)]	Zn	S	Mn	Zn	S	Mn
	Lattice Defect			Perfect Crystal		
1	1591	1465 (0.921)[b)]	27 (0.017)	1752	1637 (0.934)	26 (0.015)
2 b[c)]	1054	1023 (0.971)	13 (0.015)	1083	990 (0.914)	21 (0.019)
2'b	1200	1258 (1.048)	17 (0.014)	702	662 (0.943)	13 (0.019)
3 b	1391	1326 (0.953)	21 (0.015)	1383	1286 (0.930)	19 (0.014)
4 a	1814	1591 (0.877)	24 (0.013)	1289	1161 (0.901)	21 (0.016)
5 a	2002	1774 (0.886)	34 (0.017)	1772	1682 (0.949)	27 (0.015)
6	2179	2058 (0.944)	32 (0.015)	2047	1914 (0.935)	25 (0.012)
7 b	1632	1527 (0.936)	20 (0.012)	1739	1529 (0.879)	24 (0.014)
7'a	1345	1236 (0.919)	21 (0.016)	1446	1378 (0.953)	18 (0.012)
8 b	1085	1057 (0.974)	17 (0.016)	1327	1217 (0.917)	22 (0.017)
$\bar{x}$[d)]		0.943	0.015		0.926	0.015
σ		0.049	0.002		0.023	0.002

a) Position values are from regions having approximately the same thickness respectively.
b) Values in parentheses were normalized by the observed Zn X-ray intensities.
c) Letters "a" and "b" represent positions in which X-ray intensities on the lattice defecs were respectively smaller and larger than those in a perfect crystal region.
d) $\bar{x}$ and σ are the same as in Table 2.

Table 4 summarizes compositional analysis results at the lattice defect positions. The differences in the X-ray intensities for sulfur at the lattice defects are larger than those occurring in the perfect crystal region. In fact, the sulfur's standard deviation of X-ray intensity at the defects is twice as large as the perfect crystal's. Two patterns can be seen when the dispersion of X-ray intensity of the sulfur are compared between the lattice defect and perfect crystal regions: the normalized intensity of the sulfur at lattice defects is either larger of smaller than that at the perfect crystal region. The zinc-blende crystal structure grows in the [100] direction with the zinc and sulfur atom layers being alternately stacked. If a defect occurs in the zinc atom layer, a zinc (or sulfur) layer stacking fault is produced, thereby the variation of stoichiometry on the faults occurs. This results in the sulfur atom layer defect having a similar fault. The stacking faults are consequently classified as sulfur atom (a) and zinc atom (b) faults. Table 5 summarizes the resultant average of X-ray intensity and standard deviation for the sulfur and zinc atom faults, and clearly shows the differences in the stacking fault patterns.

〔3〕 CBED and LACBED Patterns

Stacking faults were also investigated using CBED observations which contained a higher order Laue zone (HOLZ) line patterns dependent on unit cell dimension variations. HOLZ pattern observations contrastively showed different patterns on the lattice defect regions and on perfect crystal ones. These HOLZ patterns enable changes in the lattice parameters to be observed. Figure 5 shows the HOLZ-line patterns in CBED patterns obtained with a 30 nm convergent electron beam on the exposed positions ((a)-(e)) shown in Fig. 6, whereas Table 6 summarizes the characteristic X-ray intensities simultaneously observed. These results indicate that the stacking faults in Fig. 6 are sulfur atom faults. Figure 7 shows simulated $[3\ 13\ \bar{2}]$ zone-axis HOLZ-line patterns on various lattice parameters at an accelerating voltage of 208.6 kV,[6,9] where the sample is assumed to have a cubic crystal system. The strain around the lattice defect is estimated via the varied lattice parameter in a cubic system without regard to strain direction or the unit cell distortion. The effective accelerating voltage (208.6 kv) was determined by matching the simulated HOLZ-line pattern with the experimental pattern obtained from a pure ZnS bulk crystal. Table 7 summarizes the observed lattice parameters which were determined by matching the simulated HOLZ-line pattern with

Table 5 Averaged sulfur X-ray intensities and standard deviations normalized by the observed Zn X-ray intensities for "a" and "b" in Table 4.

	a		b	
	Fault	Perfect	Fault	Perfect
$n^{a)}$	3	3	5	5
$\bar{x}$	0.894	0.926	0.976	0.917
σ	0.022	0.029	0.043	0.024

a) n is the number of data.
$\bar{x}$ and σ are the same as in Table 2.

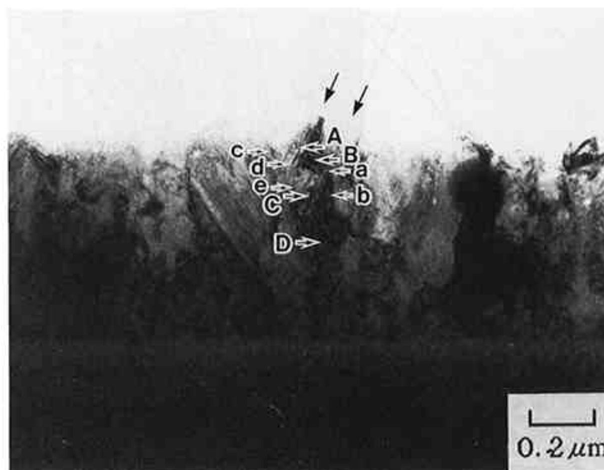

Fig. 6 Positions exposed by the convergent electron beam around the lattice defects for the observation of CBED patterns and EDS experiments. EDS elemental analyses results are summarized in the Table 6. The largest arround indicate the lattice defect positions.

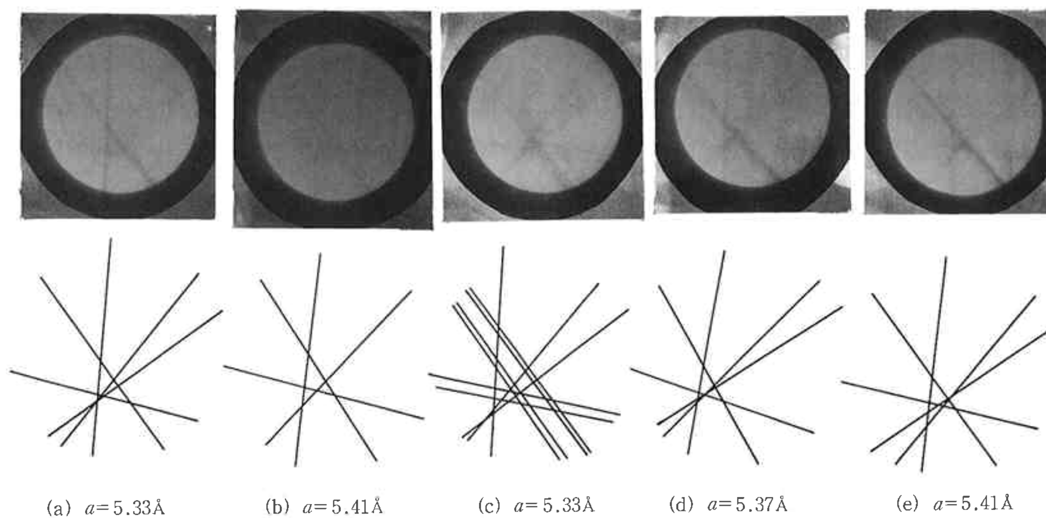

Fig. 5 Observed HOLZ-line patterns in CBED of positions (a)-(e) of Fig. 6. The exposed electron beam diameter is ~30 nm.

Table 6 Observed X-ray intensities from a ZnS:Mn thin film.

Position[a)]	Zn	S	Mn
A	1345	1236 (0.919)[b)]	21 (0.016)
B	1446	1378 (0.953)	18 (0.012)
C	1632	1527 (0.936)	20 (0.012)
D	1739	1529 (0.879)	24 (0.014)

a) Position letters correspond to the observed positions in Fig. 6.

b) Values in parentheses were normalized by the observed Zn X-ray intensities.

Table 7 Observed lattice parameters by CBED.

Position[a)]	a/Å[b)]
a	5.33
b	5.41
c	5.33
d	5.37
e	5.41

a) Position letters correspond with those in Figs. 5 and 6.

b) Values are calculated on the imaginative assumption that the crystal has a cubic crystal system.

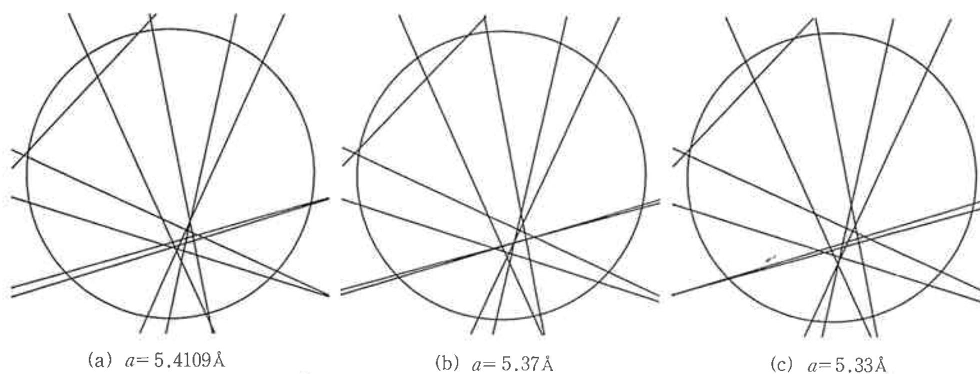

Fig. 7 Simulated [3 13 $\bar{2}$]zone-axis HOLZ-line patterns on various lattice parameters. Calculations were performed using an assumed cubic crystal system and effective accelerating voltage of 208.6 kV.

the experimental one. The effective voltage of 208.6 kV was also confirmed due to the lattice parameter in the perfect crystal region agreeing with that in the ZnS bulk crystal. Since the cubic system's reduced lattice parameters are smaller for a lattice defect than for the perfect crystal region, the lattice near the lattice defects is diminished. It should be noted that the 30 nm diameter beam is too large to expose only lattice defects. Because the beam exposes the strain region around the lattice defects, the lattice parameters are reflected by this strain field, i. e., the strain around the defects compresses and distorts them. Using the lattice defect compositional analysis results, the zinc atoms are believed to be condensed on the stacking faults; thereby causing the zinc atoms to repulse each other. Since the crystal regions near the lattice defects are compressed by this repulsive force, the lattice length is then also compressed. Additionally, the lattice energy around the lattice defects would be increased, and since this energy is supplied for bonding, the bond energy is increased and the lattice bond distance is once again reduced. The sulfur atom faults detected in Table 4 may be same as this phenomenon.

The lattice defect region which contains the lattice strain was observed by LACBED, with the resultant LACBED pattern around the lattice defects being shown in Fig. 8.. Since the sample were shifted shortly in the TEM field, the lines indicated by the arrows did not shift, and may therefore be the diffraction line, i. e., the Bragg condition is satisfied exactly on this line. The lines which almost perpendicularly intersect this line are lattice defects. If the sample was not distorted, the diffraction line would be sharp and straight, yet here it is broad and somewhat notched. This broadening indicates the existence of lattice strain around the defects, while the notches are caused by defects which cutoff crystal growth. This is another factor indicating the presence of lattice defects and lattice strain.

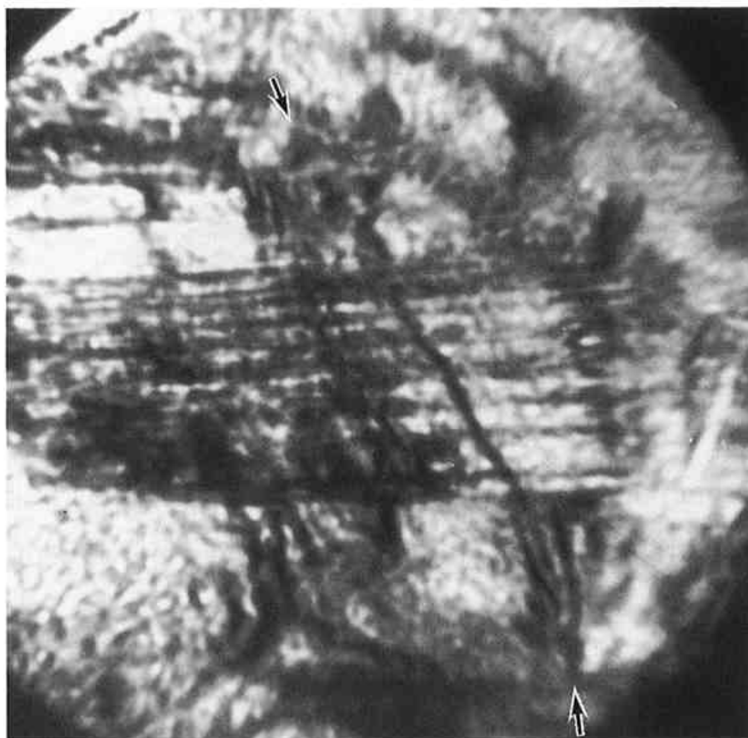

Fig. 8 LACBED pattern taken around the lattice defects. The arrows indicate the diffraction line.

4. Conclusions

Microscopic observations and elemental analyses were performed on ZnS:Ms thin films, with three different types of lattice defects being detected by both the HRTEM image and by the selected-area electron diffraction pattern made by EB deposition. The existence of two fault types, i. e., those in the layers of the zinc and sulfur atoms, was evident from the EDS elemental analyses on a sample made by MOCVD. Lattice parameters, determined by HOLZ-line patterns in CBED patterns of lattice defects, suggested the presence of a compression-type strain around the defects which subsequently causes lattice distortion. Lattice strain around the lattice defects was also observed by broadening of diffraction line obtained form the LACBED pattern. The occurrence of ZnS crystal structure variations in the two known polytypes are believed to produce the lattice defects.

The authors wish to thank Koji Shibuya and Toshiya Takahara (Advanced Materials Research Laboratory, TOSOH Corp.) for providing experiment samples, and Katsuhiko Ibe (JEOL) for the HRTEM observations.

References

1) G. DESTRIAU; *J. Chim. Phys. Phys. -Chim. Biol.* (Paris), **33**, 620 (1936).
2) For example, S. SHINOYAMA and H. KOBAYASHI (ed.); *Electroluminescence (Proc. 4th Int. Workshop Tottori)*, Tottori, 1988 (Spriner-Ferlag, Berlin,1989).
3) L. C. QIN, D. X. LI and K. H. KUO; *Philos. Mag., Sect. A,* **53**, 543 (1986).
4) Z. SHUYUAN, G. CHANGXIN, L. BILIN, and T. SHUN; *Philos. Mag., Sect. A,* **62**, 387 (1989).
5) R. W. CARPENTER and R. W. SPENCE; *Acta Crystallogr., Sect. A,* **38**, 55 (1982).
6) M. TANAKA and M. TERAUCHI; *"Convergent-Beam Electron Diffraction",* Tokyo: JEOL-Maruzen (1985).
7) R. D. SHANNON and C. T. PREWITT; *Acta Crystallogr., Sect, B,* **25**, 925 (1969).
8) R. D. SHANNON; *Acta Crystallogr., Sect. A.,* **32**, 751 (1976).
9) M. TANAKA, M. TERAUCH, and T.

KANEYAMA; "*Convergent-Beam Electron Diffraction II*", Tokyo: JEOL-Maruzen (1988).

著　者

氏名　石川芳光
Yoshimitsu ISHIKAWA
入社　平成元年４月１日
所属　東京研究センター
解析研究部

著　者

氏名　樋口眞次
Shinji HIGUCHI
入社　昭和59年９月15日
所属　東京研究センター
解析研究部
主任研究員

著　者

氏名　中西泰夫
Yasuo NAKANISHI
入社　昭和40年４月１日
所属　東京研究センター
解析研究部
部長